Journal of Applied Physics ARTICLE pubs.aip.org/aip/jap

Investigation of the solar cell materials Cu(In,Ga)Se_2 and Cu_2ZnSnS_4 with muon spin spectroscopy and density-functional calculations

Cite as: J. Appl. Phys. **136**, 055704 (2024); doi: 10.1063/5.0205837
Submitted: 28 February 2024 · Accepted: 12 July 2024 ·
Published Online: 1 August 2024

View Online Export Citation CrossMark

R. C. Vilão,[1,a)] A. G. Marinopoulos,[1] D. G. Santos,[1] H. V. Alberto,[1] J. M. Gil,[1] P. W. Mengyan,[2] M. Kauk-Kuusik,[3] J. S. Lord,[4] and A. Weidinger[5]

AFFILIATIONS

[1]CFisUC, Department of Physics, University of Coimbra, Coimbra, Portugal
[2]Department of Physics, Northern Michigan University, Marquette, Michigan MI 49855-5301, USA
[3]Department of Materials and Environmental Technology, Tallinn University of Technology, Tallinn, Estonia
[4]ISIS Facility, Rutherford Appleton Laboratory, Didcot, Oxon, UK
[5]Department ASPIN, Helmholtz-Zentrum Berlin für Materialien und Energie, Berlin, Germany

Note: This paper is part of the special topic, Defects in Semiconductors 2024.
[a)]**Author to whom correspondence should be addressed:** ruivilao@uc.pt

20 October 2025 08:59:39

ABSTRACT

Cu(In,Ga)Se_2 (CIGS) and Cu_2ZnSnS_4 (CZTS) are potential absorber materials for solar cell applications. We report an investigation of these materials using muon spin spectroscopy. In these experiments, positive muons produced at accelerator facilities (here the ISIS Facility, Rutherford Appleton Laboratory, U.K.) are implanted into the material and come to rest at interstitial sites in the host lattice. The muon is a sensitive local probe to study materials properties on an atomistic level. An advantage of the method is that interface properties can be studied by placing the probe particles at different depths in the sample. Muonium, the positive muon with an electron, can be considered as a light isotope of hydrogen (mass ratio 1/9) with almost identical electronic properties to hydrogen. Thus, muon spectroscopy provides also information about hydrogen in the host material. The aim of the present experiment is to obtain information about the muonium/hydrogen states formed in CIGS and CZTS solar cell materials. A major goal of the experiment is to obtain information about the physical embedding process of the implanted particle into the host lattice. The present study combines experimental measurements with total energy calculations in the framework of density functional theory. We obtain the final configurations of muonium in CZTS, that we discuss in parallel to those in CIGS. This allows us to deepen our understanding of the influence of the hydrogen impurity on the properties of these materials. We also discuss the final steps in the process of muon implantation in these materials.

© 2024 Author(s). All article content, except where otherwise noted, is licensed under a Creative Commons Attribution (CC BY) license (https://creativecommons.org/licenses/by/4.0/). https://doi.org/10.1063/5.0205837

I. INTRODUCTION

Chalcopyrite I–III–VI_2 semiconductors constitute an important family of compound materials under intense investigation and development as solar cell absorbers with a favorable range of bandgaps for absorption of solar spectrum.[1–8] Recent efforts imply partial substitution of In by Ga [Cu(In,Ga)Se_2, CIGS], allowing photovoltaic devices with efficiencies up to 23.3%.[4,6] The search for new materials based on earth-abundant elements has prompted many efforts on the kesterite I_2–II–IV–VI_4 counterparts, of which Cu_2ZnSnS_4 (CZTS) is the most notable member.[6,9,10]

Both chalcopyrite and kesterite semiconductor compounds are characterized by the abundant presence of intrinsic defects, which are known to deeply affect the electrical properties of the materials and the corresponding efficiency of the related devices.[11] Moreover, the growth methods usually employed to obtain the final compounds imply the incorporation of a non-negligible amount of

© Author(s) 2024

hydrogen.[12–14] Hydrogen implantation in chalcopyrite-based solar cells has been performed in order to improve structural stability,[15] passivate electrically active defects and to alter locally the device conductivity to *n*-type character.[16] Fermi-level pinning at the p/n heterojunction interface of CIGS devices was also partially attributed to hydrogen defect centers, suggesting that hydrogen can impact the open-circuit voltage and device efficiencies.[17]

Most experimental information on the microscopic configurations of hydrogen in semiconductors has been obtained by modeling hydrogen with muonium, a lighter hydrogenic particle with a positive muon as the nucleus, in the framework of muon spin spectroscopy.[18–21]

Muon spin spectroscopy (μSR) is based on the implantation of muons (which in this case are generated at the Rutherford Appleton Laboratory in the U.K.) with a kinetic energy of typically 4 MeV into the sample. The muons are a sensitive probe of the local environment. In the experiment, the time evolution of the muon spin polarization is recorded via radioactive decay.[22]

Early muon spin spectroscopy studies in the chalcopyrite compounds $CuInSe_2$ and $CuInS_2$ revealed the presence of a positively charged Mu^+ configuration, bound to an anion,[23] whose diffusion behavior was later intensively studied.[24] An associated transient paramagnetic configuration, with an extremely reduced electronic spin-density at the muon, was also identified in these early studies.[25]

In a recent μSR experiment, the p/n interface of a chalcopyrite solar cell configuration was investigated. In this case, low-energy (keV) muons were used which allow depth-resolved measurement.[26–28] A defect layer with a width of about 50 nm was identified in the chalcopyrite absorber material near the interface. In this near-interface region, the lattice is more distorted than further inside the sample. The disturbance is reduced when a buffer layer is applied.

In the present study, the detailed structure of the final formed states in CIGS and CZTS is investigated. The theoretically predicted configurations are compared with experimental findings. In the experiment, also the formation probabilities of the final states are measured. A major goal of the experiment is also to obtain information about the embedding process of the implanted particle into the host lattice.

II. THEORY: DFT CALCULATIONS

The calculations were based on spin-polarized density-functional theory (DFT)[29,30] employing the VASP computational code.[31–33] For the defect calculations, a supercell approach was adopted where a single hydrogen atom was embedded in bulk-crystalline periodic cells representing the tetragonal chalcopyrite $CuInSe_2$ (CIS) and kesterite Cu_2ZnSnS_4 (CZTS) solids. 64-atom supercells with three-dimensional periodicity were constructed through a $2 \times 2 \times 1$ repetition of the conventional 16-atom tetragonal unit cell of either of these compounds. CIGS supercells with a stoichiometry of $Cu(In_{1-x},Ga_x)Se_2$ ($x = 0.1875$) were also modeled with the addition of Ga atoms at selected In sites of the lattice; see Ref. 34 for more details.

The DFT calculations were carried out using a plane-wave basis limited by a kinetic energy cutoff of 420 eV in order to represent the valence-electron wave functions with the core-valence interaction described by pseudopotentials. Such an approach was also adopted in the vast majority of existing DFT-based calculations of bulk and defect properties of the CIS and CZTS compounds.[35–42] Although, the pseudopotential approximation may introduce errors at large negative electron-binding energies deep in the valence band it has been proved to be sufficiently accurate to describe chemical bonding in solids and to provide reliable defect-formation energies. Nonetheless, an explicit all-electron methodology would clearly benefit defect studies in chalcopyrite and kesterite compounds ensuring a more refined representation of the inner-valence and core electron densities as well as the bonding between the d-electron metals with the Se and S non metals.

A semi-local DFT functional and a hybrid-functional approach were employed to describe exchange and correlation effects. The semi-local DFT functional originally proposed by Perdew, Burke, and Ernzerhof (PBE)[43] was used initially to treat the structural relaxation for the defect calculations sampling the configurational space of possible hydrogen positions for both its neutral-paramagnetic ($q = 0$) and charged-diamagnetic ($q = +1$ and $q = -1$) states. However, the final results presented here were obtained by the screened hybrid HSE06 functional[44,45] taking care to minimize any residual forces present from the optimization with the PBE functional. The use of HSE06 corrects a number of shortcomings of local and semi-local DFT functionals by admixing a portion of exact non-local Hartree–Fock exchange to the (semi) local exchange of the former. A recent systematic study of several chalcopyrite and kesterite compounds showed that the HSE06 functional reproduces very well the experimental bandgaps of these materials.[17] Non-local exchange fractions of 30.5% and 25% for CIS and CZTS, respectively, led to bandgaps of 1.04 and 1.48 eV, for these two compounds in excellent agreement with experiments.[7,8] The second-order hyperfine tensor A_{ij} was calculated for the neutral paramagnetic hydrogen states by means of the HSE06 functional adopting an implementation described in Ref. 46.

This tensor appears in the hyperfine Hamiltonian $H_{\rm hf}$,

$$H_{\rm hf} = \vec{S}_{\rm e} \cdot \mathbf{A} \cdot \vec{S}_{\rm p}, \tag{1}$$

which describes the interaction of the spin of the unpaired electron, $\vec{S}_e$, with the magnetic moment of the proton (muon) spin $\vec{S}_p$. The hyperfine tensor can be formally decomposed into isotropic and anisotropic (dipolar) parts,[47]

$$\mathbf{A} = A_{\rm iso}\,\mathbf{I} + \mathbf{D}, \tag{2}$$

with $\mathbf{I}$ being a 3×3 unit matrix. The isotropic part of this tensor, A_{iso}, also known as the Fermi-contact term is a measure of the localization of the unpaired electron of the neutral hydrogen (muonium) species. A_{iso} is proportional to the magnitude of the electron spin density, ρ_s ($\rho_s = \rho_\uparrow - \rho_\downarrow$) at the site of the hydrogen (muon) nucleus, $\mathbf{R}$ and is obtained as[47]

$$A_{\rm iso} = \frac{8\pi}{3}\, g_e \mu_e g_H \mu_H \rho_s(\mathbf{R}), \tag{3}$$

where g_e is the electron g-factor, μ_e the Bohr magneton, g_H the hydrogen nuclear gyromagnetic ratio and μ_H its nuclear magneton.

20 October 2025 08:59:39

© Author(s) 2024

For muonium the corresponding A_{iso} value (similarly the dipolar part) is obtained, instead, by multiplying with the muon gyromagnetic ratio $g_\mu \sim 3.18 g_H$.[18]

A. Crystal structure and sites

The crystal structure of both the CIGS chalcopyrite and the CZTS kesterite compound is based on the tetragonal chalcopyrite lattice,[48] which is a distorted zinc-blende lattice. This is displayed in Fig. 1 where it can be seen that the cation sublattice comprises different metal atoms. The chalcopyrite lattice contains two structural anomalies with respect to an ideal zinc-blende lattice;[49,50] these originate from the tetragonal distortion of the lattice cell quantified by the ratio of the lattice constants where $\eta = c/2a$ is different from 1 (tetragonal deformation), as well as from local distortions due to the anion displacements away from the ideal zinc-blende sites. Therefore, both tetrahedral and hexagonal interstitial sites in chalcopyrite lattices should be regarded as approximate high-symmetry sites.

In the present connection, we emphasize the hexagonal arrangement of the atoms and the hexagonal channel in the ⟨110⟩ direction (Fig. 1). As we will see later, the muon diffuses along this rather open channel at the end of its trajectory and comes to rest at specific sites in this channel. The cage enclosed by two inclined hexagons plays a special role for the final localization of the muon. Two such cages have to be distinguished, one which contains the cation-caged tetrahedral interstitial site ($T_{Cu/In}$ for CIGS or $T_{Cu/Sn/Zn}$ for CZTS) and one with the corresponding anion-caged site (T_{Se} in CIGS or T_S in CZTS).

B. Hydrogen configurations

The first aim of the DFT calculations has been to resolve all possible minimum-energy hydrogen/muonium configurations, given the ability of the μSR technique to sample not just the ground state but also higher-energy states through their hyperfine signature.[18,34] The calculations consisted of structural optimization and atomic relaxation of the respective supercells with a single hydrogen atom embedded therein. The formation energies, $E_{form}(H^q)$, of the distinct hydrogen configurations are defined as excess energies[51] with respect to the standard reference states of the solid-defect system, namely, the bulk-crystalline compound and the hydrogen gas. These energies were obtained from HSE06 calculations of the respective quantities. The corresponding expression is given as follows:

$$E_{form}(H^q) = E_{tot}(H^q) - E_{tot}(\text{bulk}) - \mu_H + qE_F, \quad (4)$$

where $E_{tot}(H^q)$ is the total energy of the supercell containing a single hydrogen atom and E_{tot}(bulk) the total energy of the defect-free bulk CIS (or CZTS) supercells. E_F is the Fermi-level position in the bandgaps commonly given with respect to the valence-band (VB) maximum, E_V, of the bulk supercell. The quantity μ_H is the chemical potential of hydrogen and it was taken as half of the total energy of an isolated hydrogen molecule at T = 0 K. This choice corresponds to hydrogen-rich conditions.

The evaluation of the energetics adopted here is based on a zero-temperature formalism and, thus, neglects vibrational-entropy contributions that can contribute to the absolute free energies. The aim of the present study has been, instead, to identify stable minimum-energy hydrogen configurations and not to determine explicitly their energetics with respect to temperature.

Hydrogen in its positively-charged ($q = +1$) diamagnetic state was found to occupy preferentially the bond-centered positions at the Cu–anion bonds for both CIS and CZTS. On the other hand, in the hydride (negatively charged hydrogen) configurations hydrogen occupied anti-bonding (AB) sites of the cation–anion bonds of the host. This state, however, is not relevant in the present context since it is unlikely that Mu^- is formed in this experiment for the following reason: during the deceleration of the implanted muon, the equilibrium charge distribution disfavors the formation of Mu^- compared to the formation of Mu^+ and Mu^0, and after stopping, no electrons are available for capture in these p-type materials. In contrast, the neutral (paramagnetic) state, H^0, exhibits a multitude of distinct configurations that for the case of the CIS compound and CIGS were discussed in our previous study.[34]

For CZTS, the two lower-energy paramagnetic H^0 configurations are depicted in Figs. 2(b) and 2(c), together with the projection of the atom arrangement along the ⟨110⟩ direction of the CZTS lattice [Fig. 2(a)]. The configuration depicted in Fig. 2(b) is an atomic-like configuration with the hydrogen nucleus residing at an interstitial position near the geometrical cation-caged tetrahedral site (T_C) of the CZTS lattice (approx. 0.45 Å away). A zero-point energy of 0.17 eV was obtained for this configuration. It can be seen that there is a sizeable spin-electron density centered at the hydrogen nucleus with a strong isotropic 1s-type electron character. However, considerable residual spin density is also distributed at the nearest Cu and S neighbors, indicating that the presence of hydrogen polarizes its immediate environment. Hyperfine calculations provided a hyperfine coupling with a magnitude of 376 MHz for the isotropic Fermi-contact term, A_{iso}, that corresponds to about 26% of the vacuum free-atom value.

The lowest-energy H^0 configuration at $T = 0$ K is anion-bound and is shown in Fig. 2(c). Its defect-formation energy is about 110 meV lower with respect to the atom-like configuration described earlier. Consideration of the zero-point vibrational

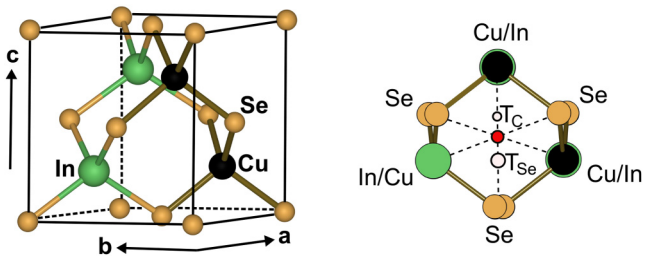

FIG. 1. Left: conventional unit cell of the tetragonal chalcopyrite lattice with a zincblende-based structure, emphasizing the hexagon arrangement of the atoms. Right: view into the hexagon channel along the ⟨110⟩ direction, depicting cation and anion columns, the interstitial hexagonal sites (red circle in the middle) and the two tetrahedral sites of the cation (Cu/In) (T_C) and selenium anion sub-lattices (T_{Se}). For CZTS, the cation columns along the ⟨110⟩-type directions are populated by Sn and Zn at an 1 : 1 ratio, instead of In.

20 October 2025 08:59:39

© Author(s) 2024

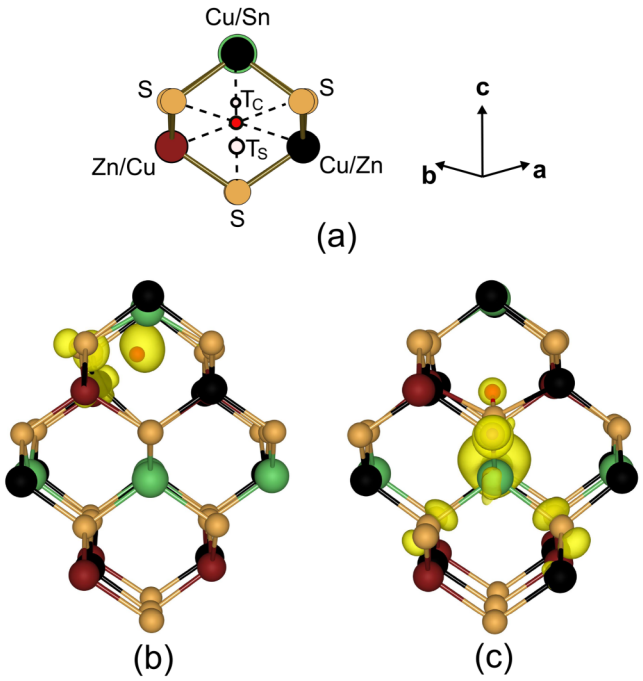

FIG. 2. (a) Projection of the atom arrangement along the ⟨110⟩ direction of the CZTS lattice, including the interstitial hexagonal sites (red circle in the middle) and the two tetrahedral sites of the cation (Cu/Sn/Zn) (T_C) and sulfur anion sublattices (T_S). (b) Atomic-like interstitial hydrogen configuration in CZTS. (c) Bound (AB Sn–S) hydrogen configuration in CZTS. The spin-electron densities are depicted in yellow with the iso-surface density magnitude set at 0.005 $e^-/Å^3$. The hydrogen nucleus is shown as the small red sphere.

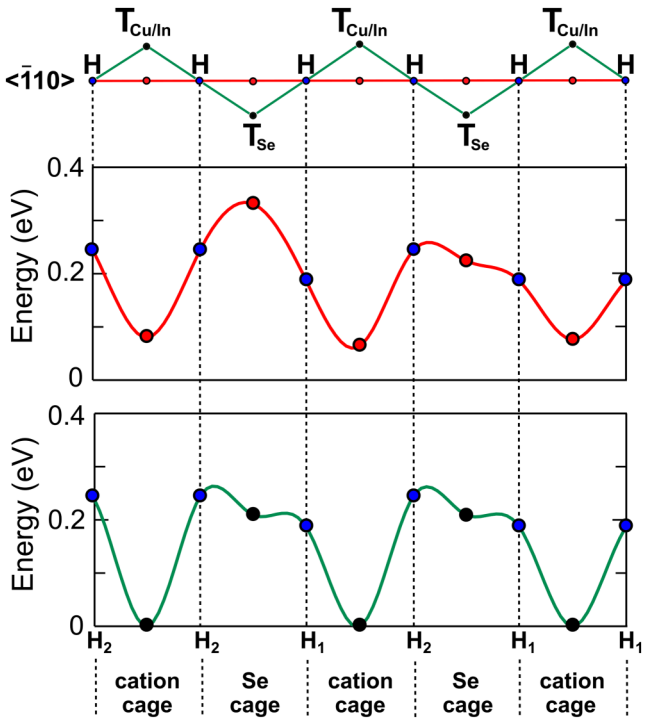

FIG. 3. Energy profiles along the ⟨−110⟩ channel for high-symmetry sites in the CIS lattice. In the upper part, a linear pathway is defined by the central axis connecting the hexagonal interstitial sites (H_1 and H_2) indicated through the centers of the hexagons (blue dots). Two consecutive hexagons define a cage, one containing the Cu/In tetrahedral site ($T_{Cu/In}$) and one the Se tetrahedral site (T_{Se}). The lower pathway is a zig-zag type with hydrogen/muonium visiting the tetrahedral sites of the respective cages.

contributions (the zero-point energy was found equal to 0.22 eV) did not change the energy ordering, nonetheless, it lowered the energy difference with the atomic-like state to about 50 meV. This bound configuration consists of hydrogen occupying the antibonding (AB) site of the host Sn–S bond; hydrogen is bonded to a S atom forming a short S–H bond (with a bond length of 1.37 Å). The corresponding electron-spin density for this bound configuration has, instead, a strong polaronic character with the largest contribution localised on the Sn atom and with smaller parts also found at Se atoms nearby. Nonetheless, there remains some residual electron density centered on the hydrogen nucleus, giving rise to a small hyperfine isotropic interaction with an A_{iso} magnitude equal to 127 MHz (∼9% of the vacuum value of the free hydrogen atom).

C. Diffusion along the hexagonal channels

We assume that at the end of the implantation trajectory, neutral muonium is captured in the hexagonal channel and diffuses along the channel axis with the remaining kinetic energy. The site changes of the light particle are still too fast for the heavier host atoms to react to it, thus it can be assumed that the particle diffuses in a frozen lattice. This assumption is also strengthened by the conservation of linear momentum at this stage of the muonium motion which favors unobstructed paths that avoid direct collision with the atoms of the host lattice.

In order to gain some insight on the basic interactions of the neutral hydrogen/muonium particle while diffusing inside the frozen-lattices of the CIGS and CZTS solids, DFT-HSE06 total-energy calculations were carried out by means of a constrained-path approach:[52] the hydrogen atoms were placed at a sequence of high-symmetry sites tracing selected continuous pathways within the hexagonal channels of the parent CIS compound. This represents good approximation for the CIGS material since it is known that the Ga atoms are substitutionally present in the CIS lattice and do not lead to strong distortions of the interatomic distances.[34]

We first consider the linear path along the channel axis connecting the interstitial hexagonal sites of CIS: this path is defined by the centers of the hexagons with a sixfold coordination (two distinct H_1 and H_2 sites for CIS) and the interstitial sites between two consecutive hexagons in the Cu/In cage and Se cage, respectively (see Fig. 3). A corresponding energy profile is generated through an interpolation of the exact results. An additional energy profile was also obtained by placing hydrogen along a staggered (zigzag)

20 October 2025 08:59:39

© Author(s) 2024

pathway that contains all cation (T_C) and anion (T_{Se}) tetrahedral sites within the hexagonal rings. It can be seen that the T_C sites are energy minima in the diffusion process, whereas a high-energy plateau appears in the energy landscape when the hydrogen/muonium crosses the hexagonal and T_{Se} sites. Comparable energy barriers are observed for motion along the respective paths; 0.27 eV for diffusion along the linear path vs 0.26 eV for a zigzag-type diffusion. Additional test calculations for CZTS showed that the different chemical elements led to more asymmetrical energy profiles with respect to CIS, nonetheless, the pattern of the energy landscape remained similar.

III. EXPERIMENTAL DETAILS AND RESULTS

Polycrystalline CIGS and CZTS samples were grown in the Laboratory of Photovoltaic Materials, Department of Materials and Environmental Technology, Tallinn University of Technology.

Monograin powders of CZTS were synthesized from high purity (99.999%) binary precursors. The used CuS and SnS precursor compounds were self-synthesized from Cu shots (99.999% Alfa Aesar), Sn shots (99.999% Alfa Aesar), and S pieces (99.999% Alfa Aesar) in evacuated quartz ampoules. ZnS powder (99.999% Alfa Aesar) was purchased commercially. As flux material, water-soluble potassium iodide was used with the mass ratio of liquid KI to solid CZTS equal to 1 : 0.5 (g/g). The precursors were weighed in desired amounts and ratios, mixed in a ball mill and loaded into quartz ampoules. The ampoules with powder batches were degassed under dynamic vacuum, sealed, and heated isothermally at 740 °C for 144 h. After cooling the ampoules to room temperature, the flux material was removed from batches by leaching and rinsing with distilled water. The released monograin powders were dried in a hot-air oven at 50 °C. According to EDX measurements, the chemical composition of CZTS powder was $Cu_{1.93}Zn_{1.12}SnS_{4.03}$.

CIGS monograin powders were prepared from binary compounds. Binary compounds CuSe, InSe, and Ga_2Se_3 were self-synthesized from 99.99% purity elements in evacuated quartz ampoules. As flux material, water-soluble potassium iodide was used with the mass ratio of KI to CIGS 1 : 0.7 (g/g). KI was dehydrated in the dynamic vacuum-pumping process by heating at temperatures up to 270 °C. The precursors were weighed in desired amounts and ratios, mixed in a ball mill, loaded into quartz ampoules, degassed under dynamic vacuum, sealed, and heated isothermally at 720 °C. The growth processes were stopped by cooling the ampoules to room temperature. The flux material was removed by leaching and rinsing with de-ionized water. The released monograin powders were dried in a hot-air oven at 50 °C. According to EDX measurements, the chemical composition of CIGS powder was $Cu(In_{0.79}Ga_{0.21})_{1.09}Se_{2.1}$.

Muon-spin spectroscopy measurements on these polycrystalline Cu(In,Ga)Se_2 (CIGS) and Cu_2ZnSnS_4 (CZTS) samples were undertaken at the EMU spectrometer of the ISIS Muon and Neutron Facility of the Rutherford Appleton Laboratory, in Chilton, U.K. The powdered polycrystalline samples were placed in a powder sample holder with a diameter of 25 mm and a thickness of 2 mm, adequate to stop the incoming muons. The muon beam was directed perpendicular to the surface of the sample holder. 100% spin-polarized positive muons with a kinetic energy of 4 MeV were implanted in the samples, and an external magnetic field was applied either perpendicular or parallel to the initial muon spin polarization (transverse geometry or longitudinal geometry, respectively), measuring the asymmetry in the emission direction of the decay positrons.

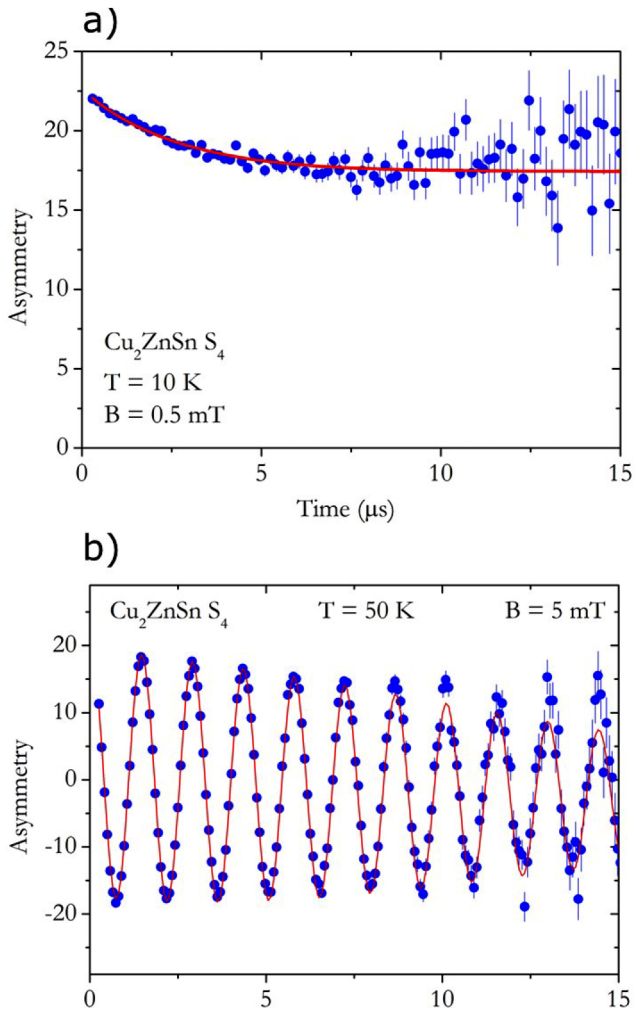

FIG. 4. (a) Longitudinal- and (b) transverse-field time spectra for Cu_2ZnSnS_4. The forward/backward asymmetry is displayed. Temperature and field values are indicated in the figures. The background signal is not subtracted. Experimental error bars for earlier times are smaller than the data points.

In the longitudinal geometry, we have explored the muon decay asymmetry as a function of the applied magnetic field, from B = 0 T up to B = 0.4 T, in order to determine the presence and strength of hyperfine interaction(s). In the transverse geometry, we have followed the temperature dependence of the spin precession of the muons in a field B = 0.5 mT. In Figs. 4(a) and 4(b), we show representative time spectra at longitudinal geometry and transverse geometry, respectively. In both cases, calibration measurements were performed with a silver sample (in order to determine the

20 October 2025 08:59:39

© Author(s) 2024

maximum instrumental asymmetry) and with a hematite (dummy) sample, in order to determine the contribution of the sample holder to the observed signal. The fraction f of muons was obtained from the experimental asymmetry A_{exp} as $f = (A_{exp} - A_{sh})/(A_{Ag} - A_{sh}) \times 100\%$, where A_{sh} is the asymmetry signal from muons stopping in the sample holder and A_{Ag} is the maximum instrumental asymmetry as determined from the calibration with silver.

In the longitudinal geometry [Fig. 4(a)], two components can be clearly separated in both samples: a relaxing component with a relaxation around $0.5\mu s^{-1}$, and a non-relaxing component; the relaxing component was found to have an exponential shape for CZTS and a gaussian shape for CIGS. The asymmetry data for the sample in the longitudinal geometry have therefore been fitted to $A(t) = A_1\exp(-\lambda t) + A_2$ in the case of CZTS) and $A(t) = A_1\exp(-\sigma^2 t^2/2) + A_2$ (in the case of CIGS). In the transverse geometry [Fig. 4(b)], asymmetry oscillation was found to be adequately described for both samples by a simple relaxing oscillation $A(t) = A\exp(-\sigma^2 t^2/2)\cos(2\pi f + \phi)$. The fits are only slightly different for the two forms of relaxation, the fit quality is almost not distinguishable in the two cases. The present data are not sufficient to clarify this question. In the present work, we, therefore, do not attribute significance to this difference.

A. Longitudinal-field decoupling experiment: Interstitial muonium

The properties of interstitial muonium can be obtained from the longitudinal-field decoupling experiment. At high magnetic fields, the muon and electron spin are decoupled and the muon spin remains aligned with the external field, i.e., it keeps its full polarization. At an intermediate field, decoupling is not complete and a transverse (relaxing) component persists. Results of an analysis with a constant and a relaxing fraction are shown in Fig. 5 for $Cu(In,Ga)Se_2$.

Above about 1 mT, the spins are completely decoupled (100% constant fraction), indicating that no strongly coupled atom-like muonium is present in $Cu(In,Ga)Se_2$. The deviations of the constant fraction from 100% at the highest fields are due to calibration uncertainties. The behavior of the fractions below about 1 mT is due to the interaction of the muon spin with nuclear magnetic moments.

In Cu_2ZnSnS_4, the compact atomic-like muonium is clearly observed (Fig. 6, where only the decoupled fraction is shown). We have fitted the data with an isotropic (A_{iso}) and a dipolar term (D) for the hyperfine interaction (red lines).[53] The results will be summarized and discussed in the discussion section.

B. Transverse-field measurement: The diamagnetic fraction

The dominant fraction in both samples is a diamagnetic component precessing at the Larmor frequency of μ^+,[18,54] corresponding to muons with no net electronic spin density at the muon position (and therefore no hyperfine interaction). Figure 7 shows the transverse-field data at 0.5 mT as a function of temperature for the two samples: $Cu(In,Ga)Se_2$ and Cu_2ZnSnS_4. The left side shows the fraction and the right side the relaxation rate.

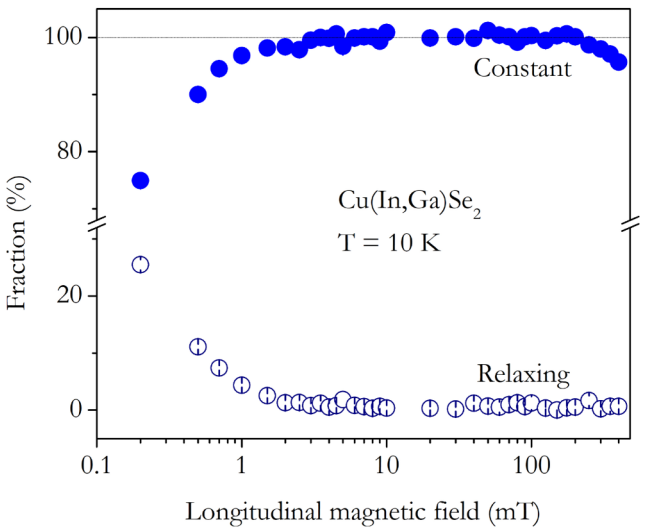

FIG. 5. Repolarization of the muon spin in $Cu(In,Ga)Se_2$ (CIGS) as a function of the external longitudinal field. The μSR time spectra were analyzed with a constant (full blue circles) and a gaussian relaxing component (open blue circles). The experimental error bars are smaller than the data points.

In both cases, the fraction reaches 100% at the highest temperatures, but clear deviations are observed at low temperatures. For $Cu(In,Ga)Se_2$ [Fig. 7(a)], almost all muons are observed in the diamagnetic component. Only at low temperatures, a small deviation from 100% occurs. We note that no muonium was observed in this sample in the decoupling experiment, thus this missing fraction is due to fast spin relaxation or dephasing before forming the final state.

For Cu_2ZnSnS_4 [Fig. 7(b)], a large missing part is observed at low temperatures. The deviation from 100% is partially due to the formation of atomic muonium (see Sec. III A), but the muonium component cannot account for the full deviation, in particular, not for the minimum at around 150 K.

The relaxation rates σ on the right side of the figures are of the order of magnitude of that expected for the interaction of the muon spin with nuclear moments. The decrease with temperature has been observed also in previous experiments and has been attributed to long-range motional narrowing followed by trapping.[24] This relaxation behavior will be discussed in more detail in the discussion (Sec. IV).

IV. DISCUSSION

This section is organized as follows: First, a model for the reaction of the muon with the host lattice is developed based on the DFT calculations. Then the formation probability and the properties of the atomic and diamagnetic state are discussed. Finally, evidence is provided for an intermediate state in the reaction pathway.

A. Reaction scheme

We now address the final thermalization step of the incoming muon. In the further discussion, we assume that the muon has

20 October 2025 08:59:39

© Author(s) 2024

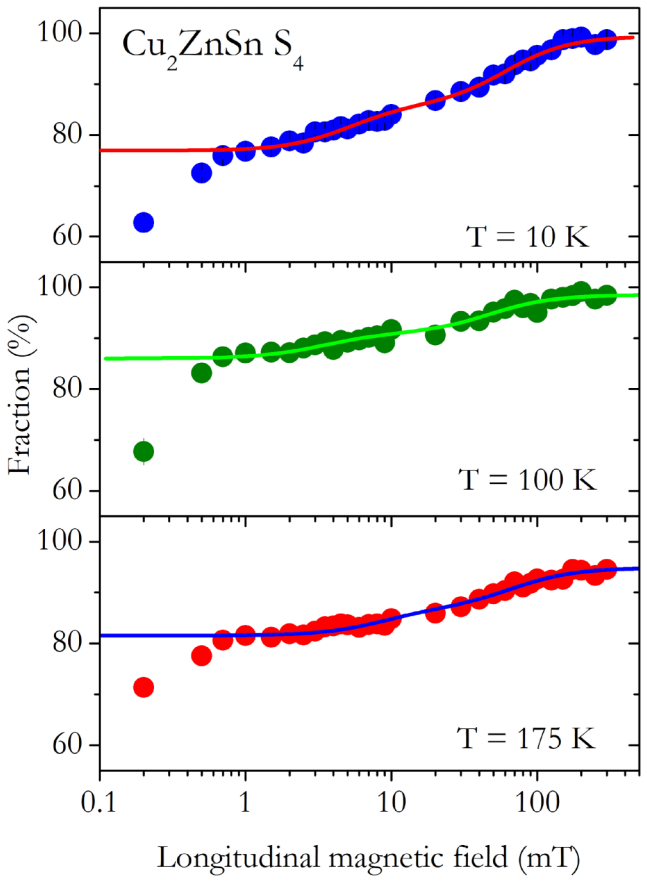

FIG. 6. Repolarization curves for Cu_2ZnSnS_4 (CZTS) in an external field at three different temperatures. The non-relaxing fraction (aligned component) is displayed. The experimental error bars are smaller than the data points. Here clearly the decoupling characteristic of compact atomic-like muonium is seen. The lines are a fit with an anisotropic hyperfine interaction. The behavior at low fields ($B < 1$ mT) is due to interaction with nuclear magnetic moments.

picked-up an electron during the deceleration and arrives at the stopping site as neutral muonium. This corresponds to the experience in other semiconductors and insulators (e.g., Ref. 55) and is due to a stronger binding of the electron to the muon than to the host atoms during the cycling charge-exchange.[56]

These incoming muonium atoms still carry some kinetic energy. At the top of the diffusion barrier, when the muonium finds itself spatially within the anion cage (see theory part), the muonium stays sufficiently long at the site to excite a local vibration.[57] A rough estimate of the time τ required to excite a high-energy phonon with the frequency ν ($\tau \sim 1/\nu$) gives that the kinetic energy should not exceed a few meV over a distance of, e.g., 0.05 nm. We assume that the final dissipation of energy occurs due to an inelastic process (excitation of a local vibration) which causes the muon to stop and the lattice atoms to adjust to the new situation. The vibration is not excited by the elastic recoil of the moving muonium, but by the force exerted by the squeezed muonium on the surrounding atoms. The primary excited vibration is a type of breathing mode with an energy at the upper end of the phonon spectrum (i.e., in the order of a few 10 meV). This energy represents a kind of "thermal spike" that can trigger reactions that are otherwise only possible at higher temperatures. We will come back to this later in the model discussion. The new potential energy profile is schematically sketched in Fig. 8, which is referring to configurations (atomic-like and bound) obtained from the DFT calculations in CZTS in Sec. II. We assume that, after being stopped by the inelastic reaction, muonium is in a transition configuration in the anion cage, from where it may convert either to an atomic-like state at an interstitial site in the cation cage or to an ionized bound configuration [at the antibonding (AB) or bond-center (BC) positions].

B. Interstitial atomic-like muonium

In CIGS, no interstitial muonium has been observed. This implies that, in the potential-energy scheme of Fig. 8, the barrier to the left side is too high and the system converts completely to the bound configuration. However, in CZTS, the atomic state has clearly been observed in the decoupling experiment. The results are summarized in Table I. We note that, for both samples, we performed as well measurements (not shown here) at low transverse magnetic fields (0.5 mT) at the lowest temperature ($T = 10$ K). The characteristic oscillations of the muonium state (here expected at around 7 MHz) were not observed in this transverse-field experiment in CZTS, indicating that the muonium state seen in the longitudinal-field experiment is either slowly formed or is fluctuating.

The values of the isotropic hyperfine interaction are approximately consistent with $A_{iso} = 1.5$ GHz with an uncertainty in the order of 0.2 GHz. The reduced hyperfine interaction $A_{iso}/A_{iso}(vac)$ is thus about 0.34(4). This value is somewhat larger than the theoretical value of 0.26 found in the DFT calculations for neutral hydrogen (Sec. II), but in the same order of magnitude.

The values of the dipolar term D and the Mu fraction vary with temperature. Note that the formation of interstitial muonium occurs from a transient state with a lower hyperfine interaction than that of interstitial muonium. The lower percentages at 100 and 175 K compared to the value at 10 K could therefore be due to dephasing, where the precursor has longer lifetimes. In the transition situation, the environment of the muon is strongly agitated so that dynamic effects could play a role also. However, no clear explanation can be derived from the available experimental data.

C. Diamagnetic fraction

The diamagnetic fraction observed in the transverse-field experiment (Fig. 7) is entirely due to the positively charged muonium Mu^+ (analog of H^+), corresponding to muons which do not interact directly with electronic spins. As mentioned in Sec. II B, the diamagnetic negatively charged Mu^- configuration can be disregarded in the context of this experiment. The major part of the diamagnetic fraction stems from muonium which has lost the electron by ionization. But, there may be also some

20 October 2025 08:59:39

© Author(s) 2024

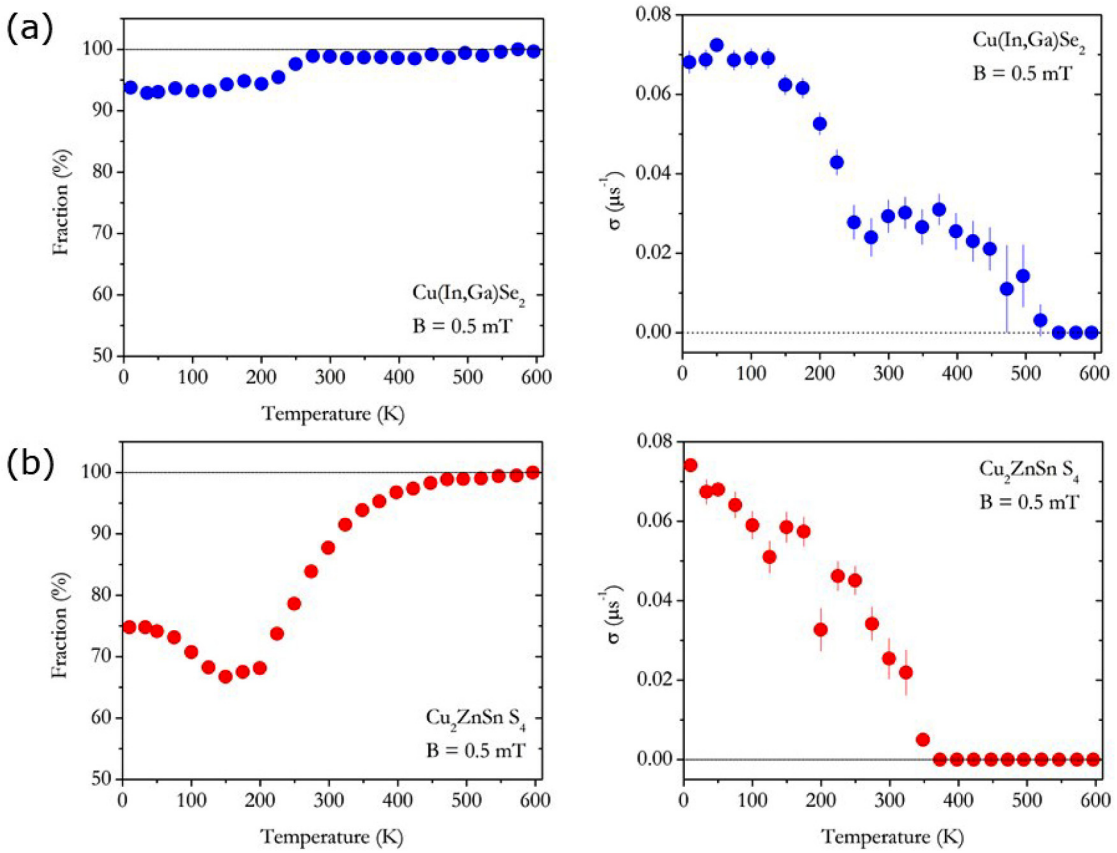

FIG. 7. Diamagnetic fraction (%) and relaxation rate σ for the two samples $Cu(In,Ga)Se_2$ (a) and Cu_2ZnSnS_4 (b) as a function of temperature in transverse magnetic field B = 0.5 mT. Most experimental error bars are smaller than the data points.

contribution from muons which have not picked-up an electron in the charge-exchange regime.[56]

We consider first the relaxation behavior of the observed diamagnetic component. The form of the temperature dependence (right side of Fig. 7) is the same as observed before[24,27] but the absolute values are somewhat lower. In these previous experiments ,relaxation rates of about $0.14\,\mu s^{-1}$ were reported. This value agrees also with calculations for the interaction with nuclear moments for a static bond of the muon to the anion (Se or S). The lower value observed now must thus be due to motional narrowing.

Considering the cage and hexagonal-channel structure of the host lattice, site changes in the cage or movement along the channel are conceivable. The sites in the interior of the cage are the antibonding positions (AB) of the cation–anion bonds in the Se/S anion cage. Due to different cations, these sites are not completely equivalent. Thus, thermally activated motion may occur in steps: starting from a bond to a single anion, averaging over two neighboring sites and finally averaging over all antibonding sites in the anion (Se or S) cage may take place. It may also be that motion along the channel is involved. No definite assignment can be made with the present knowledge.

D. Evidence for a short-lived intermediate state

A small missing fraction is observed in both samples. This indicates that some spin relaxation or dephasing takes place before or during the formation of the final states. We suggest that immediately after the inelastic reaction that leads to the stopping of the muon, an agitated lattice exists for a short time before the final states are formed. This intermediate stage can lead to polarization loss and dephasing and thus give rise to a missing fraction, as observed in other systems.[55,58]

E. μSR information and properties of the solar cell materials

As mentioned above, the μSR data can be transferred to hydrogen, thus providing information about the hydrogen defect in the two solar cell materials CIGS and CZTS. We discuss in the following some research areas, where these data may be relevant. A thorough discussion of the relationship between the μSR data and the underlying physics is not intended at this stage. (i) The hydrogen defect has always been an important topic in the field of defects in semiconductors.[18,19] It is usually argued that hydrogen is

20 October 2025 08:59:39

© Author(s) 2024

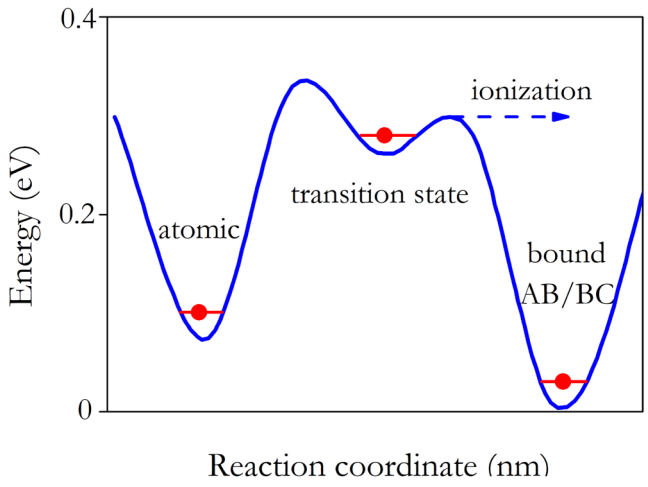

FIG. 8. Schematic (not calculated) energy profile for muonium after the stopping of the muon by the inelastic reaction. Muonium is then in a transition configuration in the anion cage. It may convert to an atomic-like state at an interstitial site in the cation cage or to an ionized bound configuration [at the antibonding (AB) or bond-center (BC) positions]. The scale of the abscissa refers to the muon positions in the different configurations.

an important defect in semiconductors and that hydrogen is a simple defect so that clear results can be obtained. Mostly theoretical data are available, while experimental verifications with direct measurements on hydrogen are rare. This is where μSR data fill the gap. The present data clearly indicate that the behavior of hydrogen in p-type materials CIGS and CZTS is dominated by the positively charged H^+ donor-like state. The isolated hydrogen impurity will therefore tend to be a compensating impurity in the pristine materials. (ii) In the introduction, we mentioned that hydrogen implantation in chalcopyrite absorber material was used to change the conduction type.[15,16] Here, our work is directly related to a practical application. Our data illustrate the final stopping and embedding of the particle in the material. This is important for the final atomistic structures that are formed and for the annealing behavior during thermal treatment. (iii) Moreover, hydrogen is likely to play as well a key role in the passivation of defects in photovoltaic devices. Chalcopyrite solar cells require buffer layers for their functioning. The best results are achieved with wet deposited CdS.[1–3] During the deposition process, Cd and possibly hydrogen diffuse into the surface area of the absorber. Understanding the passivation effect through this process is important for the technological development of these devices. The results about the mobility of the muon achieved in this work provide information about possible configuration changes in thermal treatments of the implanted materials. (iv) μSR measurements also offer the unique possibility to obtain spectroscopic information about the interface region with a depth resolution in the nanometer range. We have shown in a recent μSR experiment that a defect layer exists in the chalcopyrite absorber down to a depth of about 50 nm.[28] Different buffer layers were investigated for their annealing effect. In these μSR experiments, the muon was used as a local probe to study its environment, not as a dopant. It was found that the diamagnetic fraction is reduced when the lattice is perturbed, and the degree of reduction of the diamagnetic fraction is a measure of the magnitude of the perturbation. The present experiment provides an understanding of this effect: the barrier to ionization (right side of Fig. 8), which leads to the diamagnetic fraction, is apparently higher in a perturbed lattice than in a more perfect lattice. μSR has the potential to investigate the strain fields of interfaces in solar cells where such perturbations are expected.

TABLE I. Fit results for Cu_2ZnSnS_4 at 10K, 100, and 175 K: the isotropic hyperfine interaction A_{iso}, the dipolar term D and the muonium fraction f_{Mu}. The parameters are defined in Sec. II.

	A_{iso} (GHz)	D (GHz)	f_{Mu} (%)
10 K	1.7(2)	0.14(2)	27(1)
100 K	1.3(2)	0.09(2)	15(1)
175 K	1.9(2)	0.24(2)	16(1)

V. CONCLUSION

Information about the final steps in muon implantation in two solar cell materials has been obtained. Based on the DFT calculations the following picture is proposed: muonium (the neutral state of the muon, analog of neutral hydrogen) travels, after slowing down to almost thermal energy, along the rather open hexagonal channels in the ⟨110⟩−type directions. When the kinetic energy is sufficiently low, muonium stays sufficiently long at the saddle point of the potential energy landscape and excites a local vibration. We assume that the interaction from the muonium electron with the electrons from the host excite this local vibration via the electron–phonon interaction. This inelastic reaction leads to the final stopping of the muon and starts the incorporation of the muon in the structure of the host material.

The final configurations are either atomic-like muonium at an interstitial site or a bound muon to the anion of the host (here Se or S). The atomic-like muonium is seen in Cu_2ZnSnS_4 with a fraction in the order of 15%–30%, but is not formed in $Cu(In,Ga)Se_2$. We argue that a large energy barrier hinders or totally suppresses this reaction in the latter case. The site of atomic-like state is near the tetrahedral position in the cation cage; the hyperfine interaction is anisotropic, the isotropic part amounts to about 30% of the vacuum value.

The dominant configuration formed in this experiment is the diamagnetic Mu^+ state (an analogue of H^+), a donor-like state as expected from the behavior of a compensating impurity in these p-type semiconductors. It corresponds to a configuration with the muon bound to the anion in the antibonding direction. The electron is not bound to the muon in this configuration. Dynamics is studied via the motional narrowing of the line width. Site changes set-in above about 200 K; complete narrowing is reached at about 500 K in CIGS and 350 K in CZTS. In CIGS, clear steps in the motional narrowing are observed. We argue that local motion, i.e., jumps between different bonding positions in a cage, and the final transition to long-range diffusion can explain this behavior. In CZTS, the transition is more gradual without significant steps.

20 October 2025 08:59:39

© Author(s) 2024

In the present study, the mechanism of the stopping of the implanted particle and its embedding in the host lattices of the CIGS and CZTS compounds is clarified. This is relevant for the understanding of the often-used hydrogen implantation in semiconducting materials.

ACKNOWLEDGMENTS

The computer resources of the Department of Physics of the University of Coimbra were used, including the Navigator cluster at the Laboratory for Advanced Computing. ISIS muon beam time allocation from the Science and Technology Facilities Council, through Experiment No. RB1920408, with DOI:10.5286/ISIS.E.RB1920408, and the support of the ISIS muon team are gratefully acknowledged. This work was supported by FCT—Fundação para a Ciência e Tecnologia, I.P. through the Project Nos. UIDB/04564/2020 and UIDP/04564/2020, with DOI identifiers 10.54499/UIDB/04564/2020 and 10.54499/UIDP/04564/2020, respectively.

AUTHOR DECLARATIONS

Conflict of Interest

The authors have no conflicts to disclose.

Author Contributions

R. C. Vilão: Conceptualization (equal); Data curation (equal); Formal analysis (lead); Funding acquisition (equal); Investigation (equal); Methodology (equal); Project administration (equal); Supervision (equal); Writing – original draft (lead). **A. G. Marinopoulos:** Conceptualization (equal); Data curation (equal); Investigation (equal); Methodology (equal); Writing – original draft (lead). **D. G. Santos:** Formal analysis (lead); Investigation (equal); Writing – original draft (supporting). **H. V. Alberto:** Conceptualization (equal); Funding acquisition (equal); Investigation (equal); Methodology (equal); Validation (equal); Writing – review & editing (equal). **J. M. Gil:** Funding acquisition (equal); Investigation (equal); Methodology (equal); Supervision (equal); Validation (equal); Writing – review & editing (equal). **P. W. Mengyan:** Formal analysis (equal); Investigation (equal); Validation (equal); Writing – review & editing (equal). **M. Kauk-Kuusik:** Investigation (equal); Resources (equal); Validation (equal); Writing – review & editing (equal). **J. S. Lord:** Data curation (equal); Investigation (equal); Methodology (equal); Project administration (equal); Software (equal); Validation (equal); Writing – review & editing (equal). **A. Weidinger:** Conceptualization (equal); Investigation (equal); Methodology (equal); Supervision (equal); Writing – original draft (lead).

DATA AVAILABILITY

The data that support the findings of this study are available from the corresponding author upon reasonable request.

REFERENCES

[1]D. Abou-Ras, S. Wagner, B. J. Stanbery, H.-W. Schock, R. Scheer, L. Stolt, S. Siebentritt, D. Lincot, C. Eberspacher, K. Kushiya, and A. N. Tiwari, "Innovation highway: Breakthrough milestones and key developments in chalcopyrite photovoltaics from a retrospective viewpoint," Thin Solid Films **633**, 2 (2017).
[2]T. Feurer, P. Reinhard, E. Avancini, B. Bissig, J. Löckinger, P. Fuchs, R. Carron, T. P. Weiss, J. Perrenoud, S. Stutterheim, S. Buecheler, and A. N. Tiwari, "Progress in thin film CIGS photovoltaics–Research and development, manufacturing, and applications," Prog. Photovoltaics: Res. Appl. **25**, 645 (2017).
[3]T. Kato, "$Cu(In,Ga)(Se,S)_2$ solar cell research in solar frontier: Progress and current status," Jpn. J. Appl. Phys. **56**, 04CA02 (2017).
[4]M. Nakamura, K. Yamaguchi, Y. Kimoto, Y. Yasaki, T. Kato, and H. Sugimoto, "Cd-free $Cu(In,Ga)(Se,S)_2$ thin-film solar cell with record efficiency of 23.35%," IEEE J. Photovoltaics **9**, 1863 (2019).
[5]M. Curado, J. Teixeira, M. Monteiro, E. Ribeiro, R. Vilão, H. Alberto, J. Cunha, T. Lopes, K. Oliveira, O. Donzel-Gargand, A. Hultqvist, S. Calderon, M. Barreiros, W. Chiappim, J. Leitão, A. Silva, T. Prokscha, C. Vinhais, P. Fernandes, and P. Salomé, "Front passivation of $Cu(In,Ga)Se_2$ solar cells using Al_2O_3: Culprits and benefits," Appl. Mater. Today **21**, 100867 (2020).
[6]M. A. Green, E. D. Dunlop, M. Yoshita, N. Kopidakis, K. Bothe, G. Siefer, and X. Hao, "Solar cell efficiency tables (version 63)," Prog. Photovoltaics: Res. Appl. **32**, 3 (2024).
[7]M. Yakushev, F. Luckert, C. Faugeras, A. Karotki, A. Mudryi, and R. Martin, "Excited states of the free excitons in $CuInSe_2$ single crystals," Appl. Phys. Lett. **97**, 152110 (2010).
[8]C. Persson, "Electronic and optical properties of Cu_2ZnSnS_4 and $Cu_2ZnSnSe_4$," J. Appl. Phys. **107**, 053710 (2010).
[9]X. Cui, K. Sun, J. Huang, J. S. Yun, C.-Y. Lee, C. Yan, H. Sun, Y. Zhang, C. Xue, K. Eder, L. Yang, J. M. Cairney, J. Seidel, N. J. Ekins-Daukes, M. Green, B. Hoex, and X. Hao, "Cd-free Cu_2ZnSnS_4 solar cell with an efficiency greater than 10% enabled by Al_2O_3 passivation layers," Energy Environ. Sci. **12**, 2751 (2019).
[10]J. Zhou, X. Xu, H. Wu, J. Wang, L. Lou, K. Yin, Y. Gong, J. Shi, Y. Luo, D. Li, H. Xin, and Q. Meng, "Control of the phase evolution of kesterite by tuning of the selenium partial pressure for solar cells with 13.8% certified efficiency," Nat. Energy **8**, 526 (2023).
[11]J.-S. Park, S. Kim, Z. Xie, and A. Walsh, "Point defect engineering in thin-film solar cells," Nat. Rev. Mater. **3**, 195 (2018).
[12]S. Niki, M. Contreras, I. Repins, M. Powalla, K. Kushiya, S. Ishizuka, and K. Matsubara, "CIGS absorbers and processes," Prog. Photovoltaics Res. Appl. **18**, 453 (2010).
[13]P. Salomé, J. Malaquias, P. Fernandes, M. Ferreira, J. Leitão, A. da Cunha, J. González, F. Matinaga, G. Ribeiro, and E. Viana, "The influence of hydrogen in the incorporation of Zn during the growth of Cu_2ZnSnS_4 thin films," Sol. Energy Mater. Sol. Cells **95**, 3482 (2011).
[14]J. Park, J. Huang, J. Yun, F. Liu, Z. Ouyang, H. Sun, C. Yan, K. Sun, K. Kim, J. Seidel, S. Chen, M. A. Green, and X. Hao, "The role of hydrogen from ALD-Al_2O_3 in kesterite Cu_2ZnSnS_4 solar cells: Grain surface passivation," Adv. Energy Mater. **8**, 1701940 (2018).
[15]M. Yakushev, I. Ogorodnikov, V. Volkov, and A. Mudryi, "Incorporation of hydrogen in $CuInSe_2$: Improvements of the structure," J. Vac. Sci. Technol. A **29**, 051201 (2011).
[16]K. Otte, G. Lippold, H. Neumann, and A. Schindler, "Hydrogen in $CuInSe_2$," J. Phys. Chem. Solids **64**, 1641 (2003).
[17]J. Varley, V. Lordi, T. Ogitsu, A. Deangelis, K. Horsley, and N. Gaillard, "Assessing the role of hydrogen in Fermi-level pinning in chalcopyrite and kesterite solar absorbers from first-principles calculations," J. Appl. Phys. **123**, 161408 (2018).
[18]S. Cox, "Muonium as a model for interstitial hydrogen in the semiconducting and semimetallic elements," Rep. Prog. Phys. **72**, 116501 (2009).
[19]S. F. J. Cox, R. L. Lichti, J. S. Lord, E. A. Davis, R. C. Vilão, J. M. Gil, T. D. Veal, and Y. G. Celebi, "The first 25 years of semiconductor muonics at ISIS, modelling the electrical activity of hydrogen in inorganic semiconductors and high-κ dielectrics," Phys. Scr. **88**, 068503 (2013).
[20]J. G. Nakamura, Y. Kawakita, K. Shimomura, and T. Suemasu, "Hydrogen impurities in p-type semiconductors, GeS and GeTe," J. Appl. Phys. **130**, 195701 (2021).

20 October 2025 08:59:39

© Author(s) 2024

[21]M. Hiraishi, H. Okabe, A. Koda, R. Kadono, and H. Hosono, "Ambipolarity of diluted hydrogen in wide-gap oxides revealed by muon study," J. Appl. Phys. **132**, 105701 (2022).
[22]A. D. Hillier, S. J. Blundell, I. McKenzie, I. Umegaki, L. Shu, J. A. Wright, T. Prokscha, F. Bert, K. Shimomura, A. Berlie, H. Alberto, and I. Watanabe, "Muon spin spectroscopy," Nat. Rev. Methods Primers **2**, 4 (2022).
[23]J. M. Gil, P. J. Mendes, L. P. Ferreira, H. V. Alberto, R. C. Vilão, N. Ayres de Campos, A. Weidinger, Y. Tomm, C. Niedermayer, M. V. Yakushev, R. D. Tomlinson, S. P. Cottrell, and S. F. J. Cox, "Modeling hydrogen in $CuInSe_2$ and $CuInS_2$ solar cell materials using implanted muons," Phys. Rev. B **59**, 1912 (1999).
[24]R. C. Vilão, J. M. Gil, H. V. Alberto, J. Piroto Duarte, N. A. de Campos, A. Weidinger, M. V. Yakushev, and S. F. J. Cox, "Muon diffusion and trapping in chalcopyrite semiconductors," Phys. B **326**, 181 (2003).
[25]R. C. Vilão, H. V. Alberto, J. M. Gil, J. P. Piroto Duarte, N. Ayres de Campos, A. Weidinger, and M. V. Yakushev, "Hydrogen states in $CuInSe_2$—AμSR study," Phys. B **340-342**, 965 (2003).
[26]H. V. Alberto, R. C. Vilão, J. M. Gil, J. P. Duarte, R. B. L. Vieira, A. Weidinger, J. P. Leitão, A. F. da Cunha, M. G. Sousa, J. P. Teixeira, P. A. Fernandes, P. M. P. Salomé, K. Timmo, M. Loorits, A. Amato, H. Luetkens, T. Prokscha, A. Suter, and Z. Salman, "Muonium states in Cu_2ZnSnS_4 solar cell material," J. Phys.: Conf. Ser. **551**, 012045 (2014).
[27]H. V. Alberto, R. C. Vilão, R. B. L. Vieira, J. M. Gil, A. Weidinger, M. G. Sousa, J. P. Teixeira, A. F. da Cunha, J. P. Leitão, P. M. P. Salomé, P. A. Fernandes, T. Törndahl, T. Prokscha, A. Suter, and Z. Salman, "Slow-muon study of quaternary solar-cell materials: Single layers and $p-n$ junctions," Phys. Rev. Mater. **2**, 025402 (2018).
[28]H. V. Alberto, R. C. Vilão, E. F. M. Ribeiro, J. M. Gil, M. A. Curado, J. P. Teixeira, P. A. Fernandes, J. M. V. Cunha, P. M. P. Salomé, M. Edoff, M. I. Martins, T. Prokscha, Z. Salman, and A. Weidinger, "Characterization of the interfacial defect layer in chalcopyrite solar cells by depth-resolved muon spin spectroscopy," Adv. Mater. Interfaces **9**, 2200374 (2022). https://doi.org/10.1002/admi.202200374
[29]P. Hohenberg and W. Kohn, "Inhomogeneous electron gas," Phys. Rev. **136**, B864 (1964).
[30]W. Kohn and L. Sham, "Self-consistent equations including exchange and correlation effects," Phys. Rev. **140**, A1133 (1965).
[31]G. Kresse and J. Hafner, "*Ab initio* molecular dynamics for liquid metals," Phys. Rev. B **47**, 558 (1993).
[32]G. Kresse and J. Hafner, "*Ab initio* molecular-dynamics simulation of the liquid-metal–amorphous-semiconductor transition in germanium," Phys. Rev. B **49**, 14251 (1994).
[33]G. Kresse and J. Furthmüller, "Efficient iterative schemes for *ab initio* total-energy calculations using a plane-wave basis set," Phys. Rev. B **54**, 11169 (1996).
[34]A. G. Marinopoulos, R. C. Vilão, H. V. Alberto, E. F. M. Ribeiro, J. M. Gil, P. W. Mengyan, M. R. Goeks, M. Kauk-Kuusik, and J. S. Lord, "Hydrogen states in mixed-cation $CuIn_{(1-x)}Ga_xSe_2$ chalcopyrite alloys: A combined study by first-principles density-functional calculations and muon-spin spectroscopy," Philos. Mag. **101**, 2412 (2021).
[35]Ç. Kılıç and A. Zunger, "Doping of chalcopyrites by hydrogen," Appl. Phys. Lett. **83**, 2007 (2023).
[36]C. Persson, Y.-J. Zhao, S. Lany, and A. Zunger, "n-type doping of $CuInSe_2$ and $CuGaSe_2$," Phys. Rev. B **72**, 035211 (2005).
[37]R. Nagoya, R. Asahi, R. Wahl, and G. Kresse, "Defect formation and phase stability of Cu2ZnSnS4 photovoltaic material," Phys. Rev. B **81**, 113202 (2010).
[38]S. Botti, D. Kammerlander, and M. A. L. Marques, "Band structures of Cu_2ZnSnS_4 and $Cu_2ZnSnSe_4$ from many-body methods," Appl. Phys. Lett. **98**, 241915 (2011).
[39]A. Walsh, S. Chen, S.-H. Wei, and X.-G. Gong, "Kesterite thin-film solar cells: Advances in materials modelling of Cu_2ZnSnS_4," Adv. Energy Mater. **2**, 400 (2012).
[40]L. E. Oikkonen, M. G. Ganchenkova, A. P. Seitsonen, and R. M. Nieminen, "Vacancies in $CuInSe_2$: New insights from hybrid-functional calculations," J. Phys.: Condens. Matter **23**, 422202 (2011).
[41]J. Pohl and K. Albe, "Intrinsic point defects in $CuInSe_2$ and $CuGaSe_2$ as seen via screened-exchange hybrid density functional theory," Phys. Rev. B **87**, 245203 (2013).
[42]J. Bekaert, R. Saniz, B. Partoens, and D. Lamoen, "Native point defects in $CuIn_{1-x}Ga_xSe_2$: Hybrid density functional calculations predict the origin of p- and n-type conductivity," Phys. Chem. Chem. Phys. **16**, 22299 (2014).
[43]J. Perdew, K. Burke, and M. Ernzerhof, "Generalized gradient approximation made simple," Phys. Rev. Lett. **77**, 3865 (1996).
[44]J. Heyd and G. Scuseria, "Efficient hybrid density functional calculations in solids: Assessment of the Heyd–Scuseria–Ernzerhof screened Coulomb hybrid functional," J. Chem. Phys. **121**, 1187 (2004).
[45]J. Paier, M. Marsman, K. Hummer, G. Kresse, I. Gerber, and J. Angyan, "Screened hybrid density functionals applied to solids," J. Chem. Phys. **124**, 154709 (2006).
[46]K. Szász, T. Hornos, M. Marsman, and A. Gali, "Hyperfine coupling of point defects in semiconductors by hybrid density functional calculations: The role of core spin polarization," Phys. Rev. B **88**, 075202 (2013).
[47]J. Spaeth and H. Overhof, *Point Defects in Semiconductors and Insulators*, Springer Series in Materials Science (Springer, 2003).
[48]S. P. Ramkumar, Y. Gillet, A. Miglio, M. J. van Setten, X. Gonze, and G.-M. Rignanese, "First-principles investigation of the structural, dynamical, and dielectric properties of kesterite, stannite, and PMCA phases of Cu_2ZnSnS_4," Phys. Rev. B **94**, 224302 (2016).
[49]J. Jaffe and A. Zunger, "Theory of the band-gap anomaly in ABC2 chalcopyrite semiconductors," Phys. Rev. B **29**, 1882 (1984).
[50]C. Schnohr, H. Kämmer, C. Stephan, S. Schorr, T. Steinbach, and J. Rensberg, "Atomic-scale structure and band-gap bowing in $Cu(In,Ga)Se_2$," Phys. Rev. B **85**, 245204 (2012).
[51]C. Freysoldt, B. Grabowski, T. Hickel, J. Neugebauer, G. Kresse, A. Zanotti, and C. V. de Walle, "First-principles calculations for point defects in solids," Rev. Mod. Phys. **86**, 253 (2014).
[52]C. Herring, N. M. Johnson, and C. G. Van de Walle, "Energy levels of isolated interstitial hydrogen in silicon," Phys. Rev. B **64**, 125209 (2001).
[53]F. L. Pratt, "Repolarization of anisotropic muonium in orientationally disordered solids," Philos. Mag. Lett. **75**, 371 (1997).
[54]B. Patterson, "Muonium states in semiconductors," Rev. Mod. Phys. **60**, 69 (1988).
[55]R. C. Vilão, A. G. Marinopoulos, H. V. Alberto, J. M. Gil, J. S. Lord, and A. Weidinger, "Sapphire $\alpha-Al_2O_3$ puzzle: Joint μSR and density functional theory study," Phys. Rev. B **103**, 125202 (2021).
[56]M. Senba, D. J. Arseneau, J. J. Pan, and D. G. Fleming, "Slowing-down times and stopping powers for $\sim$2-MeVμ^+ in low-pressure gases," Phys. Rev. A **74**, 042708 (2006).
[57]V. Dzhagan, A. P. Litvinchuk, M. Y. Valakh, and D. R. T. Zahn, "Phonon Raman spectroscopy of nanocrystalline multinary chalcogenides as a probe of complex lattice structures," J. Phys.: Condens. Matter **35**, 103001 (2023).
[58]R. C. Vilão, R. B. L. Vieira, H. V. Alberto, J. M. Gil, and A. Weidinger, "Role of the transition state in muon implantation," Phys. Rev. B **96**, 195205 (2017).

20 October 2025 08:59:39

© Author(s) 2024